Inorganic Chemistry

Article

pubs.acs.org/IC

High-Temperature Phase Transitions, Spectroscopic Properties, and Dimensionality Reduction in Rubidium Thorium Molybdate Family

Bin Xiao,[†,‡] Thorsten M. Gesing,[§] Philip Kegler,[†] Giuseppe Modolo,[†] Dirk Bosbach,[†] Hartmut Schlenz,[†] Evgeny V. Suleimanov,[⊥] and Evgeny V. Alekseev*[,†,‡]

[†]Institute for Energy and Climate Research (IEK-6), Forschungszentrum Jülich GmbH, 52428 Jülich, Germany

[‡]Institut für Kristallographie, RWTH Aachen University, 52066 Aachen, Germany

[§]Chemische Kristallographie fester Stoffe, Institut für Anorganische Chemie, Universität Bremen, Leobener Straße, D-28359 Bremen, Germany

[⊥]Department of Chemistry, Lobachevsky State University of Nizhny Novgorod, 603950, Nizhny Novgorod, Russia

Supporting Information

ABSTRACT: Four new rubidium thorium molybdates have been synthesized by high-temperature solid-state reactions. The crystal structures of $Rb_8Th(MoO_4)_6$, $Rb_2Th(MoO_4)_3$, $Rb_4Th(MoO_4)_4$, and $Rb_4Th_5(MoO_4)_{12}$ were determined using single-crystal X-ray diffraction. All these compounds construct from MoO_4 tetrahedra and ThO_8 square antiprisms. The studied compounds adopt the whole range of possible structure dimensionalities from zero-dimensional (0D) to three-dimensional (3D): finite clusters, chains, sheets, and frameworks. $Rb_8Th(MoO_4)_6$ crystallizes in 0D containing clusters of $[Th(MoO_4)_6]^{8-}$. The crystal structure of $Rb_2Th(MoO_4)_3$ is based upon one-dimensional chains with configuration units of $[Th(MoO_4)_3]^{2-}$. Two-dimensional sheets occur in compound $Rb_4Th(MoO_4)_4$, and a 3D framework with channels formed by thorium and molybdate polyhedra has been observed in $Rb_4Th_5(MoO_4)_{12}$. The Raman and IR spectroscopic properties of these compounds are reported. Temperature-depended phase transition effects were observed in $Rb_2Th(MoO_4)_3$ and $Rb_4Th(MoO_4)_4$ using thermogravimetry-differential scanning calorimetry analysis and high-temperature powder diffraction methods.

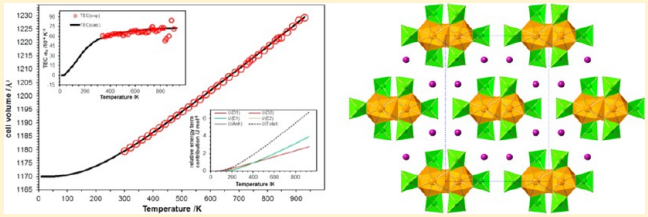

1. INTRODUCTION

The modern industrialized world's thirst for energy has stimulated progressive researches into diverse energy substitutes. Future electricity generation will need a range of options, which must all be low in carbon if greenhouse gas emissions are to be reduced. Among numerous substitutes, nuclear energy provides a reliable supply of electricity with very low carbon emissions and relatively small amounts of waste that can be safely stored and eventually disposed in a final repository. Currently, the most common nuclear fuel supplied for nuclear reactors is based on uranium. Nevertheless, a number of concerns have been raised about using uranium as an energy source, which eventuates in an increasing interest in thorium as a possible alternative to uranium in next nuclear fuel generations. The thorium fuel cycle has some attractive features, though it is not yet in commercial use. Thorium is reported to be 3 times more abundant in the earth crust than uranium. With regard to proliferation significance, thorium-based power reactor fuels would be a very poor source for fissile material usable in the illicit manufacture of nuclear weapons.[1] The application of thorium in a nuclear reactor involves a large array of chemical interactions among fission products with nuclear fuel, leading to the formation of complex thorium compounds, which in turn affects the integrity and behavior of fuel. Therefore, knowledge of the chemical properties of these thorium compounds becomes the necessary prerequisite for utilizing this promising energy.

Molybdenum is one of the significant fission products created with high yield in a nuclear reactor.[2] In addition, actinide molybdates may be considered as important materials for long-term evolution of a geological repository for spent nuclear fuel.[3] In the past few decades, extended studies on radioactive molybdate compounds have been conducted on high-valent uranium(VI) phases containing approximately the linear uranyl cation UO_2^{2+}.[4] By comparison, sparser chemical studies have been reported for lower-valent actinide molybdate compounds such as Th(IV), Np(IV), and Pu(IV). The first published thorium molybdate example is orthorhombic $Th(MoO_4)_2$.[5] The crystal structure of this compound was later derived by Thoret.[6] It consists of only one crystallographic Th cation position, which is coordinated by eight molybdate tetrahedra oxygen atoms. The initial work on quaternary thorium molybdate compounds containing alkali metals has been explored and studied by Tabuteau and Pages[7] using micro thermal analysis and powder X-ray diffraction. Thereafter, the crystal structures of a series of thorium molybdate compounds, namely, $K_2Th(MoO_4)_3$ and $K_4Th(MoO_4)_4$ as well as K_8Th-

Received: December 5, 2013
Published: March 6, 2014

   dx.doi.org/10.1021/ic403003f | Inorg. Chem. 2014, 53, 3088−3098

Table 1. Crystallographic Data of $Rb_8Th(MoO_4)_6$, $Rb_2Th(MoO_4)_3$, $Rb_4Th(MoO_4)_4$, $Rb_4Th_5(MoO_4)_{12}$

compound	$Rb_8Th(MoO_4)_6$	$Rb_2Th(MoO_4)_3$	$Rb_4Th(MoO_4)_4$	$Rb_4Th_5(MoO_4)_{12}$
mass	1875.44	882.80	583.48	586.81
space group	$C2/c$	$C2/c$	$C2/c$	$C2/c$
a (Å)	10.7163(3)	18.1583(6)	26.889(4)	29.3907(4)
b (Å)	18.0594(4)	12.5089(3)	6.3934(1)	16.8025(2)
c (Å)	14.9941(4)	5.3882(2)	11.3566(1)	10.2016(1)
β (deg)	103.417(3)	105.058(3)	113.986(1)	101.539(1)
V (Å^3)	2822.61(13)	1181.85(7)	1783.74(4)	4936.11(10)
Z	4	4	4	4
λ (Å)	0.71073	0.71073	0.71073	0.71073
$F(000)$	3320	1544	2136	5944
μ (cm^{-1})	21.62	23.89	21.96	21.96
ρ_{calcd} (g cm^{-3})	4.413	4.961	4.519	4.604
$R(F)$ for $F_o^2 > 2\sigma(F_o^2)$[a]	0.0464	0.0349	0.0231	0.0280
$Rw(F_o^2)$[b]	0.1109	0.0571	0.0656	0.0597

[a] $R(F) = \sum||F_o| - |F_c||/\sum|F_o|$ [b] $R(F_o^2) = [\sum w(F_o^2 - F_c^2)^2/\sum w(F_o^4)]^{1/2}$

$(MoO_4)_6$ have been reported by Huyghe et al.[8] $A_4Th(MoO_4)_4$ (A = Rb, Cs) has only been studied by powder X-ray diffraction, and the structures are not known.[9] Recently, Dahale et al.[10] reported on the synthesis and thermal stability of $Na_2Th(MoO_4)_3$ and $Na_4Th(MoO_4)_4$, respectively. The thermal behavior and expansion studies of $Cs_2Th(MoO_4)_3$ and $Cs_4Th(MoO_4)_4$ have been characterized by Keskar et al.[11] using high-temperature X-ray powder diffraction and differential thermal analysis techniques. However, the detailed characterization of these compounds was barely presented. Given the importance of thorium compounds and considerable vacancies of structural research on thorium molybdate compounds, here we discuss the synthesis, crystal structure, optical properties, and thermal behavior of a novel thorium molybdate family containing rubidium cations: $Rb_8Th(MoO_4)_6$, $Rb_2Th(MoO_4)_3$, $Rb_4Th(MoO_4)_4$, and $Rb_4Th_5(MoO_4)_{12}$.

2. EXPERIMENTAL SECTION

2.1. Crystal Synthesis. All titled compounds were obtained by high-temperature solid-state reactions. Analytical reagent grade chemicals were used without further purification.

Synthesis of $Rb_8Th(MoO_4)_6$ Crystals. $Th(NO_3)_4{\cdot}5H_2O$ (Merck), $RbNO_3$ (Alfa-Aesar), and MoO_3 (Alfa-Aesar) with the molar ratio of 1:2:2 (0.10 g, 0.052 g, and 0.051 g for $Th(NO_3)_4{\cdot}5H_2O$, $RbNO_3$, and MoO_3, respectively) were thoroughly ground together and loaded into a platinum crucible. About 5% excessive amount of MoO_3 (about 2.5 mg) was added to compensate its evaporation at high temperature. The reaction mixture was then placed into a program-controlled furnace (CARBOLITE CWF 1300) and heated to 900 °C in 4 h, staying at this temperature for 10 h to secure a homogeneous reaction of the mixture. After that, slowly cooling to 400 °C at a rate of 5 °C/h was followed by a rate of 50 °C/h to room temperature. The reaction product consisted of colorless prism-like crystals. $Rb_8Th(MoO_4)_6$ can also be found as a minor product in reactions with the molar ratios of 3:1:8 (0.10 g, 0.009 g, and 0.067 g for $Th(NO_3)_4{\cdot}5H_2O$, $RbNO_3$, and MoO_3, respectively) and 3:2:5 (0.10 g, 0.017 g, and 0.042 g for $Th(NO_3)_4{\cdot}5H_2O$, $RbNO_3$, and MoO_3, respectively), respectively.

Synthesis of $Rb_2Th(MoO_4)_3$ Crystals. $Th(NO_3)_4{\cdot}5H_2O$ (0.10 g), $RbNO_3$ (0.078 g), and MoO_3 (0.101 g) (with Th/Rb/Mo molar ratio of 1:3:4) were weighted with 5% excessive amount (5 mg) of MoO_3. After it was thoroughly ground, the reaction mixture was loaded into a platinum crucible and placed into the furnace. The crucible was heated to 900 °C in 4 h, keeping at this temperature for 10 h for homogeneously melting. Then it was slowly cooled to room temperature with a rate of 5 °C/h. The major product was orthorhombic $Th(MoO_4)_2$. $Rb_2Th(MoO_4)_3$ was present in trace amounts. A few $Rb_2Th(MoO_4)_3$ crystal formed in prism-like shape and thus could be identified quite easily.

Synthesis of $Rb_4Th(MoO_4)_4$ Crystals. A mixture of $Th(NO_3)_4{\cdot}5H_2O$ (0.10 g), $RbNO_3$ (0.052 g), and MoO_3 (0.101 g) (with the Th/Rb/Mo ratio of 1:2:4) was thoroughly ground together and loaded into a platinum crucible. Following the similar procedure for $Rb_8Th(MoO_4)_6$, colorless crystals in the form of blocks and colorless amorphous phases as side products were found for the reaction.

Synthesis of $Rb_4Th_5(MoO_4)_{12}$ Crystals. $Rb_4Th_5(MoO_4)_{12}$ was prepared using $Th(NO_3)_4{\cdot}5H_2O$ (0.10 g), $RbNO_3$ (0.026 g), and MoO_3 (0.025 g). The experimental parameters were the same as those for $Rb_8Th(MoO_4)_6$. The reaction product consisted of well-formed colorless prism-like crystals and amorphous phases. $Rb_4Th_5(MoO_4)_{12}$ could also be found as a major product in the experiment with $Th(NO_3)_4{\cdot}5H_2O$, $RbNO_3$, and MoO_3 molar ratio of 1:1:3, 2:3:2, 2:3:4, and 3:2:5 (0.10 g, 0.175 mmol of $Th(NO_3)_4{\cdot}5H_2O$ for each reaction).

2.2. Preparation of Pure Phases. The pure phase powders of all four rubidium thorium molybdate compounds were prepared according to each stoichiometric ratio. $Th(NO_3)_4{\cdot}5H_2O$, $RbNO_3$, and MoO_3 were put into four plantinum crucibles with four different Th/Rb/Mo ratios (1:8:6, 1:2:3, 1:4:4, and 5:4:12; 0.2 g, 0.35 mmol of $Th(NO_3)_4{\cdot}5H_2O$ for each reaction) for $Rb_8Th(MoO_4)_6$, $Rb_2Th(MoO_4)_3$, $Rb_4Th(MoO_4)_4$, and $Rb_4Th_5(MoO_4)_{12}$, respectively. The standard procedure for pure phase synthesis was performed as follows: after being thoroughly ground, the reaction mixtures were initially heated in air up to 450 °C and kept at this temperature for 30 h. After that, the room-temperature X-ray powder diffraction was collected to analyze the phase content and purity. The same grinding and heating steps were repeated several times with 50 °C/step of temperature increasing until the pure phases were obtained. Pure phases of $Rb_8Th(MoO_4)_6$, $Rb_2Th(MoO_4)_3$, $Rb_4Th(MoO_4)_4$, and $Rb_4Th_5(MoO_4)_{12}$ were finally obtained at 450, 700, 650, and 700 °C, respectively. $Rb_8Th(MoO_4)_6$, $Rb_2Th(MoO_4)_3$, and $Rb_4Th_5(MoO_4)_{12}$ were obtained with high yields (>98%) confirmed by powder XRD (Figure SI1). The $Rb_4Th(MoO_4)_4$ synthesis always yielded ~95%, with aproximately 5% of $Rb_2Th(MoO_4)_3$ as impurity (see section 3.4 in Results and Discussion).

2.3. X-ray Powder Diffraction and Single-Crystal Structure Analysis. X-ray powder diffraction patterns were collected on a Bruker-AXS D4 Endeavor diffractometer in Bragg−Brentano geometry, equipped with a copper tube and a primary nickel filter providing Cu $K\alpha_{1,2}$ radiation (λ = 1.54187 Å). A one-dimensional silicon strip LynxEye detector (Bruker-AXS), using a voltage equal 40 kV and an electric current equal 40 mA (1.6 kW), was used. Data were recorded in the range of 2θ = 10−80° (total counting time = 10 s/step with a step width of 0.02°). The aperture of the fixed divergence slit was set to 0.2 mm, and that of the receiving slit was set to 8.0 mm. The discriminator of the detector was set to an interval 0.16 to 0.25 V. The

dx.doi.org/10.1021/ic403003f | Inorg. Chem. 2014, 53, 3088−3098

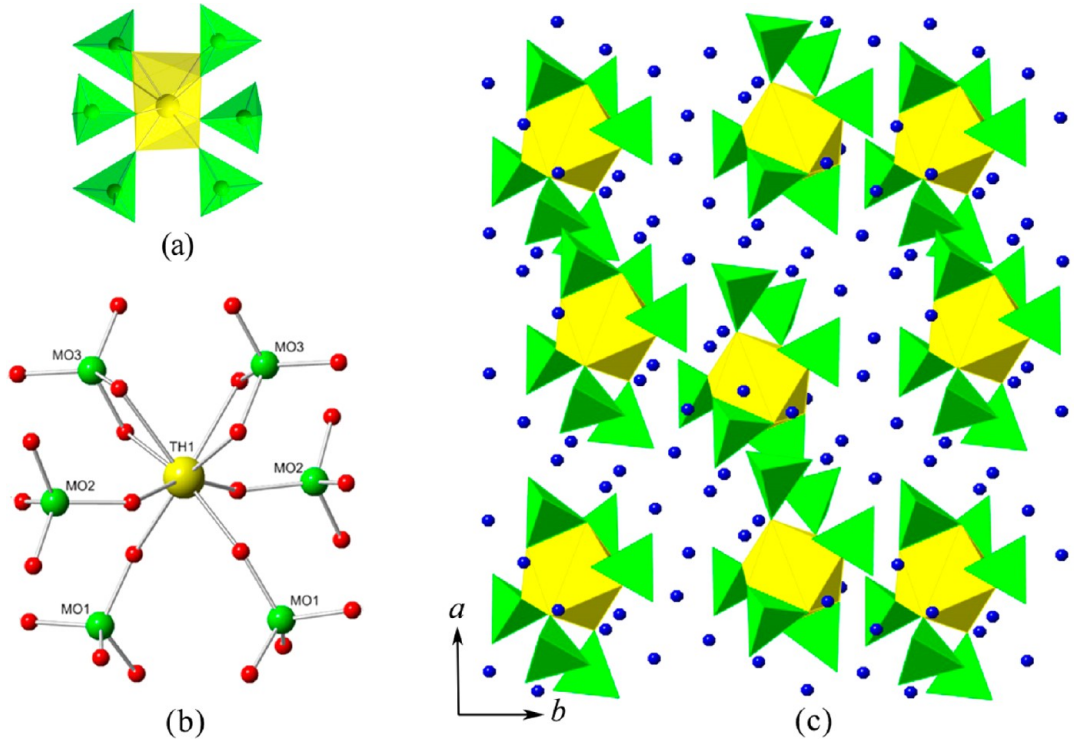

Figure 1. Depiction of finite clusters of $Rb_8Th(MoO_4)_6$. (a) The thorium molybdate cluster with composition of $[Th(MoO4)_6]^{8-}$. (b) Coordination geometry of the thorium molybdate cluster. (c) A polyhedral representation of the structure projected along [001]. The Th and Mo are drawn with yellow and green colors, respectively.

X-ray powder diffraction patterns for all four rubidium thorium molybdates are provided in the Supporting Information (Figure SI1).

The temperature-dependent X-ray powder diffraction data were collected on a Panalytical MPD powder diffractometer using Bragg–Brentano geometry. The setup was equipped with a secondary Ni filter, Cu Kα radiation, a X'Celerator multi strip detector, and an Anton Paar HTK1200N heating chamber. The sample was placed on a flat corundum holder having a small evaporation channel that served for optimum space during the thermal expansion of $PbFeBO_4$. Diffraction was carried out between 300 and 930 K, with a ramping slice of 20 K. Each diffraction pattern was recorded from 5° to 85° 2θ, with a step size of 0.0167° and a 0.5 s/step total data collection time.

The rubidium thorium molybdate single crystals selected for data collection were mounted on glass fibers and then optically aligned on an Agilent SuperNova (Dual Source) diffractometer. All data were collected using a monochromatic Mo Kα_1 tube with an incident wavelength of 0.71073 Å, running at 50 kV and 0.8 mA and providing a beam size of approximately 30 μm. The unit-cell dimensions for titled compounds were refined using least-squares techniques against the positions of all measured reflections. More than a hemisphere of data was collected for each crystal, and the three-dimensional data were reduced and filtered for statistical outliers using the standard CrysAlis^{Pro} program. Data were corrected for Lorentz, polarization, absorption, and background effects. The SHELXL-97 program was used for the determination and refinement of the structures.[12] The data and crystallographic information are given in Table 1. The structures were solved by direct methods and refined to R_1 = 0.046 for $Rb_8Th(MoO_4)_6$, R_1 = 0.035 for $Rb_2Th(MoO_4)_3$, R_1 = 0.023 for $Rb_4Th(MoO_4)_4$, and R_1 = 0.028 for $Rb_4Th_5(MoO_4)_{12}$.

2.4. Scanning Electron Microscopy/Energy-Dispersive Spectroscopy. Scanning electron microscopy images and energy-dispersive spectroscopy (SEM/EDS) data were collected on a FEI Quanta 200F Environment Scanning Electron Microscope. The EDS results are provided in the Supporting Information (Figure SI2 and Table SI1).

2.5. IR and Raman Spectroscopy. A Bruker Equinox spectrometer was used for the IR experiments, and the KBr pellet technique was applied for sample preparation. For this purpose, approximately 200 mg of KBr and 2 mg of each sample were mixed carefully, and a pressure of 10 tons was applied and held constant for 3 min to prepare each pellet. The IR spectra were recorded in the range from 400 to 4000 cm^{-1}. A pure KBr pellet, which was prepared under the same experimental conditions, was used as blank sample.

Unpolarized Raman spectra were recorded with a Horiba LabRAM HR spectrometer using a peltier-cooled multichannel CCD detector. An objective with a 50× magnification was linked to the spectrometer, allowing the analysis of samples as small as 2 μm in diameter. All the samples were in the form of polycrystalline powders. The incident radiation was produced by a He–Ne laser line at a power of 17 mW (λ = 632.81 nm). The focal length of the spectrometer was 800 mm, and an 1800 gr/mm grating was used. The spectral resolution was around 1 cm^{-1} with a slit of 100 μm. The spectra were recorded in the range of 100–1050 cm^{-1}. No photoluminescence (PL) was observed.

2.6. TG-DSC Experiments. The thermal behavior of the dried powders was studied from room temperature to 1250 °C by differential scanning calorimetry analysis (DSC) coupled with thermogravimetry (TG) in air at a heating rate of 10 °C/min using a Netzsch STA 449C Jupiter apparatus. Each sample (20 mg) was loaded in a platinum crucible, which was closed with a platinum cover. During the measurements a constant air flow of 20–30 mL/min was applied.

2.7. Bond-Valence Analysis. Bond-valence sums (BVS) for all atom positions in the four rubidium thorium molybdate phases were calculated, and the results are given in the Supporting Information (Table SI3). The bond-valence parameters for Th(IV)-O, Rb(I)-O, and Mo(VI)-O are used according to Brese and O'Keeffe.[13] The BVS for all atoms are coincident with their expected formal valence.

3. RESULTS AND DISCUSSION

3.1. Structure Description. *$Rb_8Th(MoO_4)_6$.* The crystal structure of $Rb_8Th(MoO_4)_6$ is based upon finite $[Th(MoO_4)_6]^{8-}$ clusters, as shown in Figure 1a,b. The Th centers of these clusters are linked by four monodentate MoO_4 as well

dx.doi.org/10.1021/ic403003f | Inorg. Chem. 2014, 53, 3088–3098

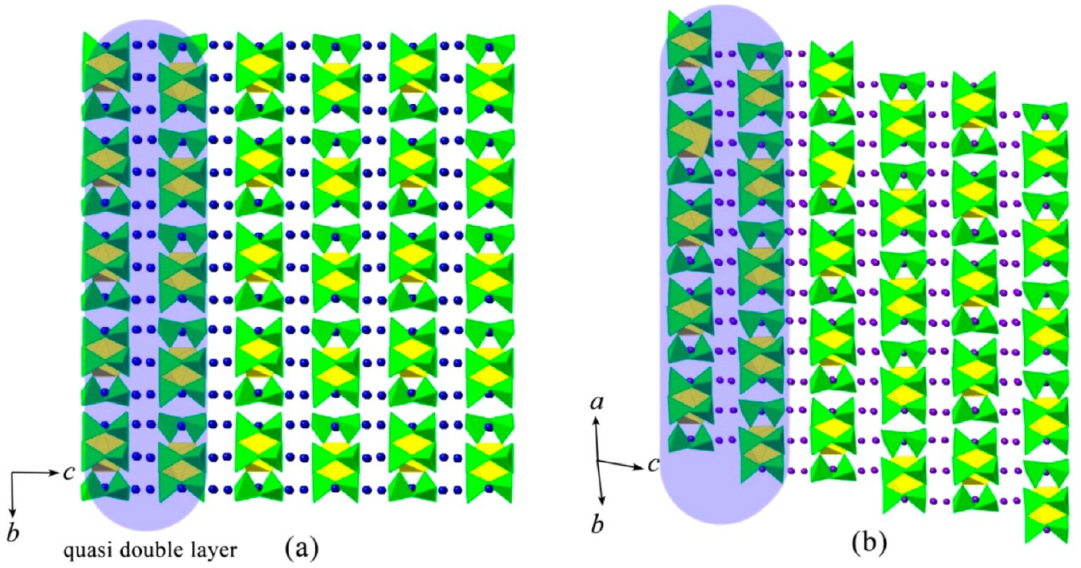

Figure 2. A view of packing modes in the structures of (a) $Rb_8Th(MoO_4)_6$ and (b) $K_8Th(MoO_4)_6$. The quasi-double layers are highlighted in both structures.

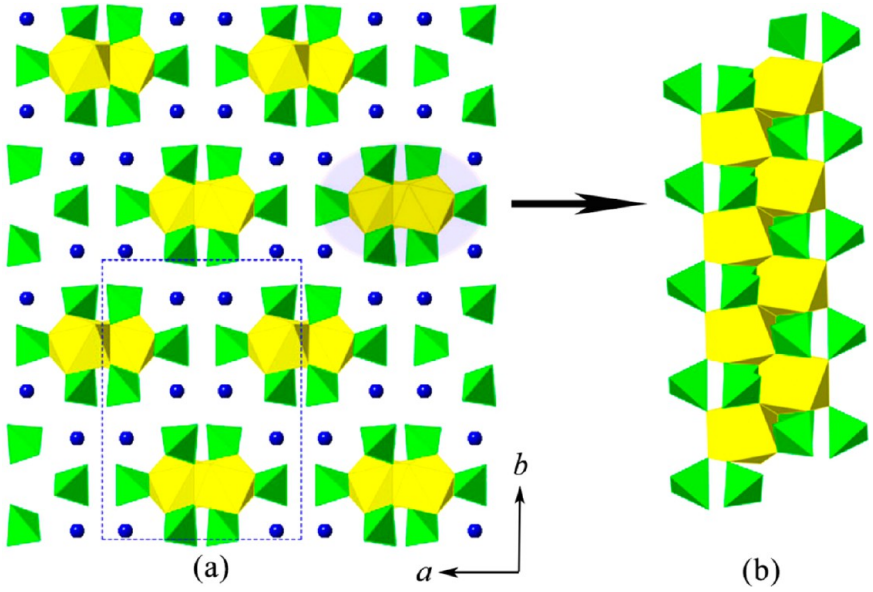

Figure 3. Depiction of one-dimensional chain of $Rb_2Th(MoO_4)_3$. (a and b) View along two different directions shows the chains with configuration of $[Th(MoO4)_3]^{2-}$.

as two bidentate MoO_4 tetrahedra. The O−Mo−O bond angles of the monodentate MoO_4 tetrahedra are found in a range from 107.0(3)° to 112.5(3)°, representing a normal deviation from the ideal tetrahedral angle of 109.4°. In the bidentate MoO_4 tetrahedra one rather small O−Mo−O angle of 95.5(2)° could be found, whereas the other angles are slightly bigger up to 116.1(3)°. The rather small tetrahedral angle is found between those two oxygen atoms (O1 and O2), which are additionally bonded to the central thorium atom showing also longer Mo−O bond distances of 1.795(5) Å (O1) and 1.804(5) Å (O2), respectively, compared to O5 (1.742(5) Å) and O3 (1.741(5) Å). The thorium molybdate clusters are separated from each other by intercalated rubidium cations, which results in zero-dimensional thorium molybdate building units (Figure 1c). $Rb_8Th(MoO_4)_6$ is the second known thorium molybdate with cluster structure. The first example is a structure of chemically similar $K_8Th(MoO_4)_6$.[8a] The structure of $K_8Th(MoO_4)_6$ also comprises the finite $[Th(MoO_4)_6]^{8-}$ clusters, which are topologically identical to those in $Rb_8Th(MoO_4)_6$. However, due to the presence of different alkali cations with different ionic radii, the packing mode of the clusters within the structures is different in K and Rb analogues, and resulting structures are not isostructural. As seen in Figure 2, the packing mode resulting in a quasi-double layer perpendicular to the crystallographic *c*-axis in $Rb_8Th(MoO_4)_6$ is shifted by half a cluster unit in the structure of $K_8Th(MoO_4)_6$. In addition, the two layers which comprise each quasi-double layer in the structure of $Rb_8Th(MoO_4)_6$ are severely twisted in the structure of $K_8Th(MoO_4)_6$. The structural difference is also reflected by the different symmetries of the two structures: triclinic for $K_8Th(MoO_4)_6$ (space group $P\bar{1}$) and monoclinic for $Rb_8Th(MoO_4)_6$ (space group $C2/c$).

dx.doi.org/10.1021/ic403003f | *Inorg. Chem.* 2014, 53, 3088−3098

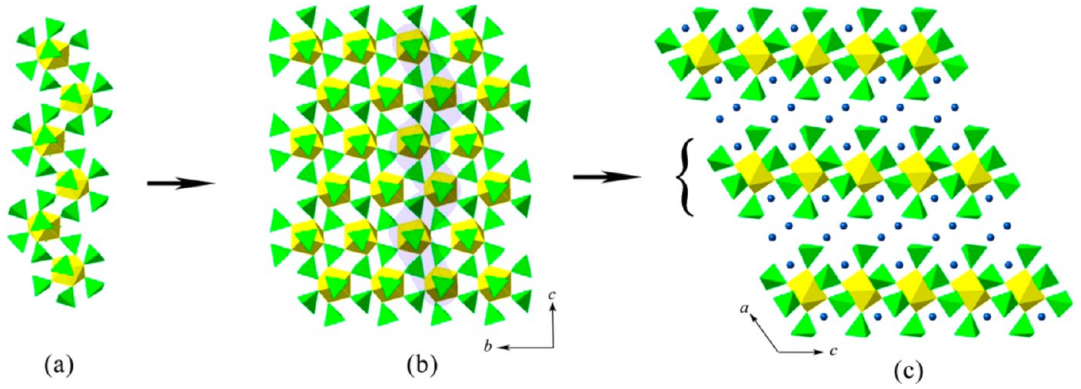

Figure 4. Depiction of 2D sheets of $Rb_4Th(MoO_4)_4$. (c) A projection along [010] direction shows that $Rb_4Th(MoO_4)_4$ is based on 2D thorium molybdate sheets. (b and a) The $[Th(MoO_4)_4]^{4-}$ chains are connected side-by-side in the same orientation propagating parallel to *y*-axis resulting in sheet.

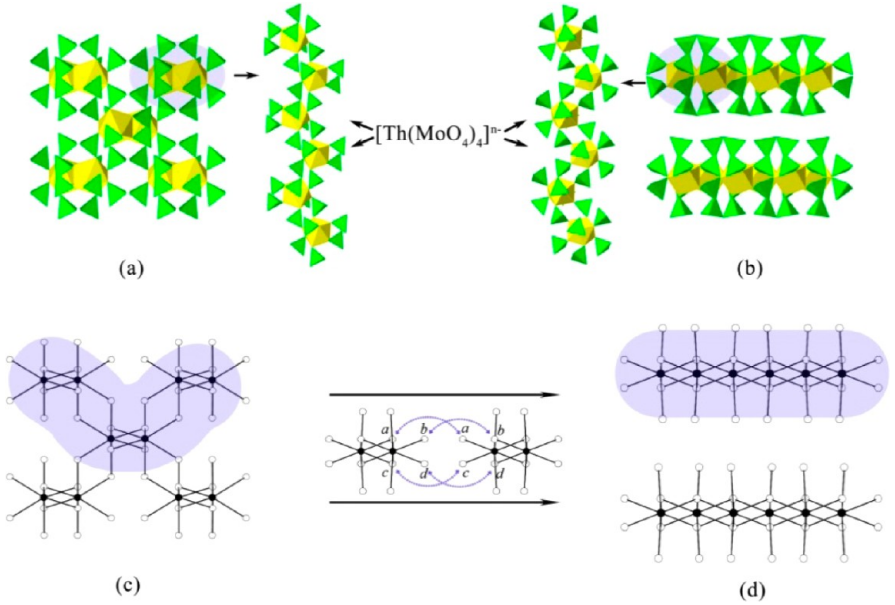

Figure 5. Chains of square antiprism and tetrahedra in different thorium molybdate compounds. (a) Framework of $Na_4Th(MoO_4)_4$ and its fundamental chains. (b) 2D structure of $Rb_4Th(MoO_4)_4$ and its fundamental chains. (c and d) Black-and-white graphs describing transformation from 3D framework to 2D chains by connecting equivalent white points labeled by same letters.

$Rb_2Th(MoO_4)_3$. The crystal structure of $Rb_2Th(MoO_4)_3$ adopts a one-dimensional chain structure as given in Figure 3. This compound crystallizes in space group *C*2/*c* and is isotypic to the $K_2Th(MoO_4)_3$ structure that can be seen as deriving from $Am_2(MoO_4)_3$, which follows the scheelite structure.[8b] In $Rb_2Th(MoO_4)_3$, the slightly distorted thorium square antiprisms share a common edge with two neighboring thorium atoms each and are surrounded by vertex-sharing MoO_4 tetrahedra to form infinite $[Th(MoO_4)_3]^{2-}$ chains (Figure 3b) oriented parallel to [001]. Each single Th site is connected to eight MoO_4 tetrahedra with Th−O distances ranging from 2.346(4) to 2.544(4) Å. It is interesting to note that thorium-based $Rb_2Th(MoO_4)_3$ has a similar structure as the corresponding lanthanide family of $KBaGd(MO_4)_3$ (M = Mo, W) compounds, which were synthesized under similar conditions.[14] Both structures can be evolved from scheelite-related $CaMoO_4$ by superseding 1/3 of Ca atoms with Th^{4+} or Gd^{3+} ions and 2/3 with alkali or alkaline-earth metals. Rb^+ ions are fully located in 8f sites within the $Rb_2Th(MoO_4)_3$ structure and are surrounded by eight oxygen atoms with bond lengths ranging from 2.837(4) to 2.967(4) Å. For lanthanide $KBaGd(MO_4)_3$, however, the monovalent K^+ and divalent Ba^{2+} ions require a partial occupancy of the same sites to accomplish the valence as well as atoms balance during replacement. The average bond distances for the ThO_8 and GdO_8 polyhedra are 2.433 and 2.420 Å in $Rb_2Th(MoO_4)_3$ and $KBaGd(MoO_4)_3$, respectively.

$Rb_4Th(MoO_4)_4$. Single-crystal X-ray diffraction studies reveal that $Rb_4Th(MoO_4)_4$ crystallizes in the monoclinic space group *C*2/*c*. $Rb_4Th(MoO_4)_4$ has been previously studied by powder X-ray diffraction;[9c] however, no structural information has been given except cell parameters. A [010] projection shows that $Rb_4Th(MoO_4)_4$ is based on two-dimensional (2D) thorium molybdate sheets (Figure 4c). Each ThO_8 square antiprism is surrounded by eight vertex-sharing MoO_4 tetrahedra. Compared to the first two structures one can separate thorium molybdate single chains within the 2D layer. These chains are based on ThO_8 square antiprisms bridged by two MoO_4 tetrahedra to form a $[Th(MoO_4)_4]^{4-}$ composition (Figure 4a). The $[Th(MoO_4)_4]^{4-}$ chains are fused side-by-side in the

dx.doi.org/10.1021/ic403003f | *Inorg. Chem.* 2014, 53, 3088−3098

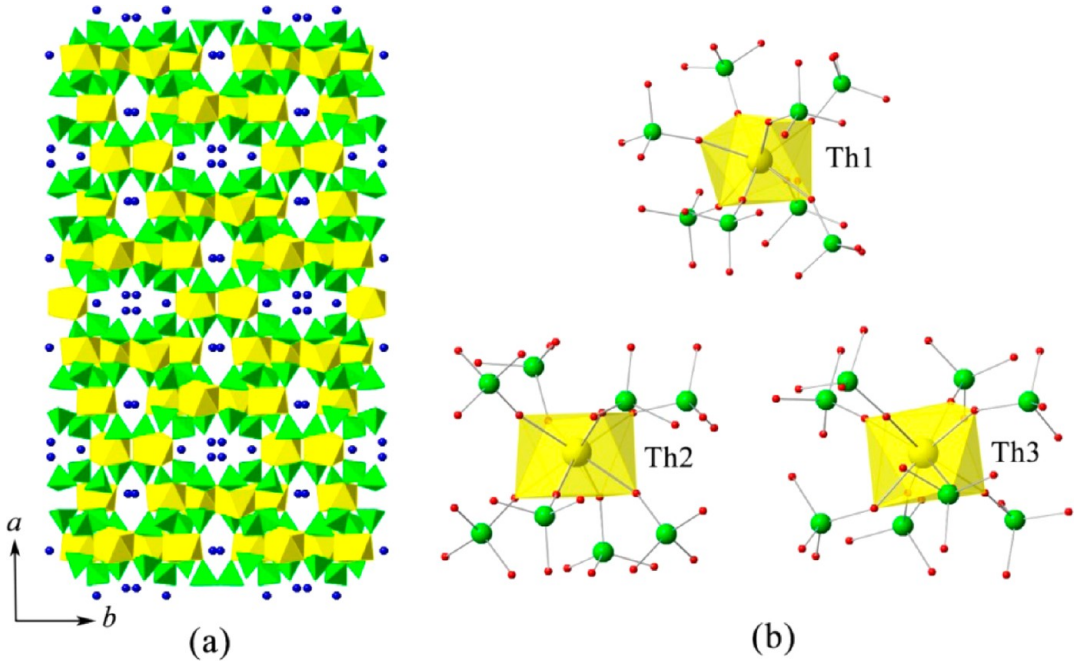

Figure 6. Depiction of 3D framework structure in $Rb_4Th_5(MoO_4)_{12}$. (a) View along *c*-axis demonstrates two kinds of channels parellel to [001] direction. (b) Coordination environment of three Th in $Rb_4Th_5(MoO_4)_{12}$. Each of the Th centers shows square antiprism geometry by connecting to eight monodentate MoO_4 tetrahedra.

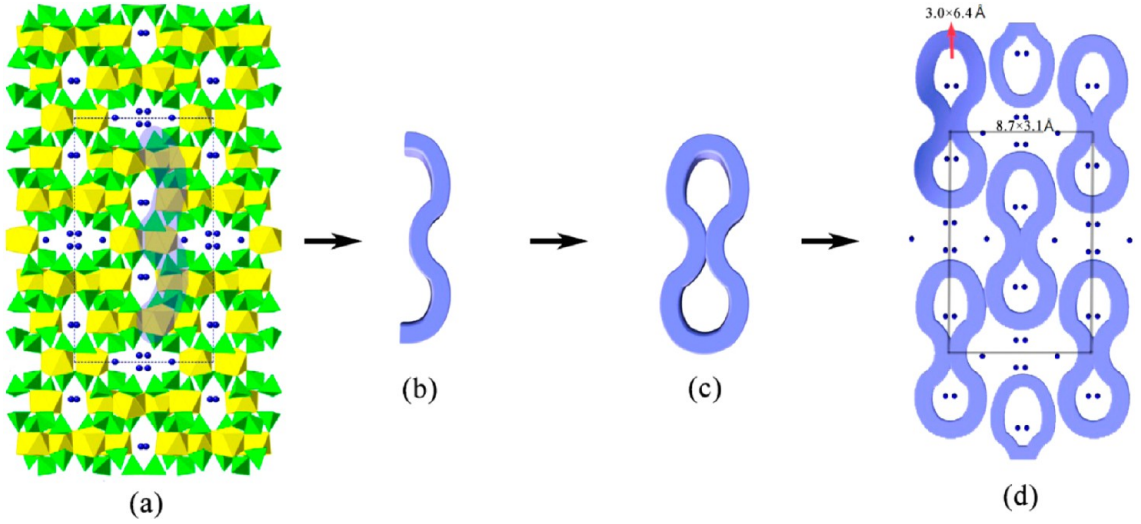

Figure 7. The process of butterfly-shaped FBB forming the channels in structure $Rb_4Th_5(MoO_4)_{12}$.

same orientation along the [010] direction, resulting in the aforementioned 2D sheets (Figure 4b). The Rb(2) cations reside within the sheets, whereas the Rb(1) cations provide a cross-link between neighboring layers, stacking parallel to the *c*-axis (Figure 4c). The building chains, $[Th(MoO_4)_4]^{4-}$, in the structure of $Rb_4Th(MoO_4)_4$, are similar to those found in the $A_4Th(MoO_4)_4$ (A = Na, K) series.[8c,10] The $Th[(MoO_4)_4]^{4-}$ chains in these structures have a similar topology as those in $Rb_4Th(MoO_4)_4$ but are different with respect to geometry. One crystallographic-independent Th site and two Mo sites occur in the chain observed in $Rb_4Th(MoO_4)_4$, whereas only one Th site and one Mo site each are found within the $K_4Th(MoO_4)_4$ chains. The average Th−O bond length in $Rb_4Th(MoO_4)_4$ is 2.407(3) Å, which is similar to that in $K_4Th(MoO_4)_4$ (2.416(3) Å).[8c] A comparison of $[Th(MoO_4)_4]^{4-}$ chain structures in $Rb_4Th(MoO_4)_4$ and in the $A_4Th(MoO_4)_4$ series is presented in Figure 5. The topology of $Rb_4Th(MoO_4)_4$ sheets and the $A_4Th(MoO_4)_4$ framework can be illustrated using a white-and-black representation where black nodes and white nodes correspond to ThO_8 square antiprisms and MoO_4 tetrahedra, respectively, as shown in Figure 5d,c. In both topologies, all black vertexes (Th sites) are 8-fold connected. Every Mo site is 2-fold connected in $A_4Th(MoO_4)_4$, whereas in $Rb_4Th(MoO_4)_4$ half of the Mo sites are 3-fold connected; the remaining Mo sites are only 1-fold connected. As a consequence, $Th[(MoO_4)_4]^{4-}$ chains lead to a three-dimensional (3D) framework in $A_4Th(MoO_4)_4$, while a layered structure results in $Rb_4Th(MoO_4)_4$. The topological transformation from the 3D framework conformation to 2D sheets can be made by using the *cutting and gluing* procedure, which involves reconstruction

dx.doi.org/10.1021/ic403003f | Inorg. Chem. 2014, 53, 3088−3098

of the local coordination of the Mo sites. First of all, the Mo−O connections within the edge side of each $Th[(MoO_4)_4]^{4-}$ fragment in the framework structure of $A_4Th(MoO_4)_4$ have to be broken to obtain a single $Th[(MoO_4)_4]^{4-}$ chain. The equivalent Mo points (white nodes) on the side of each $Th[(MoO_4)_4]^{4-}$ chain have been labeled with the letters *a*, *b*, *c*, and *d*. The topological transformation from the 3D framework to the 2D sheet structure can be completed by jointing of the corresponding white nodes *a*−*a*, *b*−*b*, *c*−*c*, and *d*−*d*, as shown in Figure 5. This transformation only involves changing the coordination number of Mo atoms, without reconstructing the topology of the $Th[(MoO_4)_4]^{4-}$ chains. Different structural arrangements with similar basic units reflects the mutable nature of Th−O−Mo linkages. Interestingly, similar $[X(MoO_4)_4]^{n-}$ chains are observed in other molybdate compounds, such as $Na_5La(MoO_4)_4$[15] or $Na_5Tb(MoO_4)_4$.[16]

$Rb_4Th_5(MoO_4)_{12}$. This compound adopts an open-framework structure type and is the most complex thorium molybdate to date (Figure 6a). It contains three symmetrically independent Th sites with coordination geometries as shown in Figure 6b. Each of the Th atoms is surrounded by eight oxygen atoms, resulting in a square antiprism geometry, and is linked to eight monodentate MoO_4 tetrahedra. All oxygen atoms in $Mo(5)O_4$ are fully bonded with Th atoms, while $Mo(1)O_4$, $Mo(2)O_4$, $Mo(3)O_4$, Mo(4)O4, and $Mo(6)O_4$ tetrahedra have one terminal oxygen atom each. The Mo−O distance ranging from 1.674(8) to 1.784(5) Å is consistent with other thorium molybdate structures involving monodentate molybdate linkages.[8c,17] The structure of $Rb_4Th_5(MoO_4)_{12}$ can be described as corrugated butterfly-shaped ribbons, which are highlighted in Figure 7a. These anionic ribbons act as the fundamental building block (FBB) of the $Rb_4Th_5(MoO_4)_{12}$ structure and consist of MoO_4 tetrahedra and ThO_8 square antiprisms. Two ribbons related by inversion transformation are connected together (Figure 7c), resulting in a porous bow-knot shaped fragment that occurs identically in the corner- and body-center of the unit cell. Within this, the pores have the internal size of 3.0 × 6.4 Å and are occupied by Rb(3) atoms. The bow-knot shaped fragments further pack into a 3D framework, which leads to large, approximately elliptical channels with inner dimensions of 8.7 × 3.1 Å, running parallel to the *c*-axis. The Rb(1) and Rb(2) atoms partially and fully reside in the center and the side of the channels, respectively. Note that the large channels in the framework of $Rb_4Th_5(MoO_4)_{12}$ may indicate its ability to host diverse cations of various radii as well as valence without considerable geometric parameters change. In other words, the Rb cations may be substituted by other ions while the structural skeleton remains unchanged. In this case $Rb_4Th_5(MoO_4)_{12}$ may be considered as an ion-exchange candidate.

3.2. Structural Dimensionality. The structural variability of the four rubidium thorium molybdates reported here is observed from a finite cluster compound to a 3D framework structure realized by corner- and edge-sharing ThO_8 square antiprisms and MoO_4 tetrahedra, respectively. The dimensionality changing in these phases can be explained using the concept of "dimensional reduction," which was first discussed by Long et al.[18] It has been shown that the structural dimensionality of metal chalcogenides decreases while increasing the ratio of electropositive cations or ionic salts.[19] Later, this method has been discussed in detail as a mean to rationalize composition-structure association in the alkali metal uranyl molybdates.[3a] Following this principle, we consider each of the rubidium thorium molybdate compounds as a member of the homologous formula $[Rb_2MoO_4]_x[Th(MoO_4)_2]_y$. The dense 3D framework orthorhombic $Th(MoO_4)_2$ is a member of the series in this expression with x/y ratio of 0.[6] With increasing x/y ratio, the dimensionality of the framework is reduced. Thus, the $Rb_4Th_5(MoO_4)_{12}$ framework at a x/y ratio of 0.4 is relatively open, with tunnels that include Rb cations. A further increase of the x/y ratio up to 2 stabilizes the 2D structure of $Rb_4Th(MoO_4)_4$, and the largest x/y ratio of 4 gives the cluster $Rb_8Th(MoO_4)_6$. The only exception here is the chain structure of $Rb_2Th(MoO_4)_3$. This deviation is due to the different connection behavior of Th in $Rb_2Th(MoO_4)_3$. There are edge-sharing Th antiprisms (Th−Th) in $Rb_2Th(MoO_4)_3$, but all the Th cations in the other three rubidium thorium molybdates are bonded to eight oxygen atoms with no Th−Th polyhedra connectivity. Essentially, as the x/y ratio increases, the dense packed lattice of the parent compound ($Th(MoO_4)_2$) is diluted by incorporated Rb atoms, which breaks the Th−O−Mo linkage and lowers the dimensionality of the rubidium thorium molybdates.

3.3. Raman and IR Spectra. Figure 8 shows the Raman spectra of $Rb_8Th(MoO_4)_6$, $Rb_2Th(MoO_4)_3$, $Rb_4Th(MoO_4)_4$, and $Rb_4Th_5(MoO_4)_{12}$. All the vibrational wavenumbers measured are located below 1050 cm^{-1}, which is typical for inorganic molybdate compounds.[20] It is obvious to coarsely divide all the spectra into two frequency parts: a low-frequency part between 100 cm^{-1} and 250 cm^{-1}, where the modes are contributed from the vibrations of the "lattice skeleton", and a high-frequency part from 300 cm^{-1} to 1000 cm^{-1}, which is assigned to the internal motions of MoO_4^{2-}. The IR spectra of all molybdate compounds in the range from 400 cm^{-1} to 1050 cm^{-1} are shown in the Supporting Information (Figure SI4). The peaks of the four compounds, in this range, are predominantly attributed to motions of MoO_4^{2-}, displaying

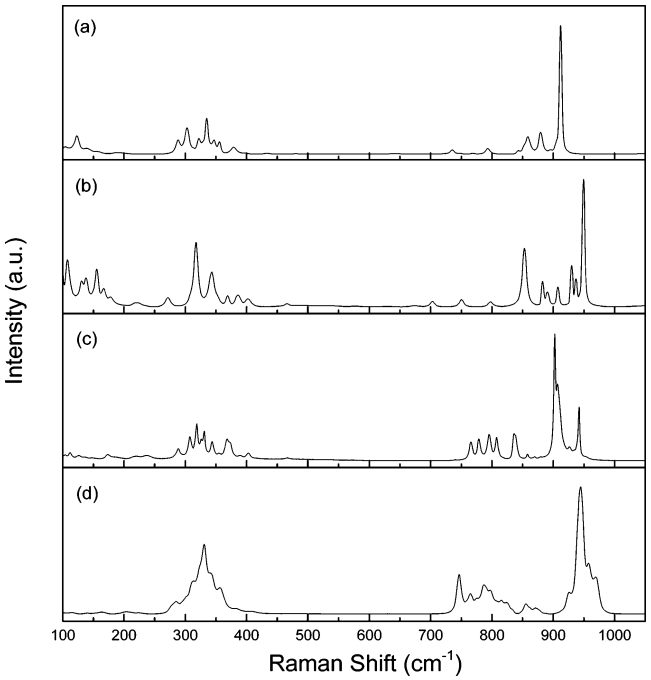

Figure 8. Raman spectra of (a) $Rb_8Th(MoO_4)_6$, (b) $Rb_2Th(MoO_4)_3$, (c) $Rb_4Th(MoO_4)_4$, (d) $Rb_4Th_5(MoO_4)_{12}$ measured from 100 to 1050 cm^{-1}.

dx.doi.org/10.1021/ic403003f | Inorg. Chem. 2014, 53, 3088−3098

Table 2. Determined Raman and IR Bands (cm^{-1}) and Proposed Band Assignments for $Rb_8Th(MoO_4)_6$, $Rb_2Th(MoO_4)_3$, $Rb_4Th(MoO_4)_4$, $Rb_4Th_5(MoO_4)_{12}$

$Rb_8Th(MoO_4)_6$		$Rb_2Th(MoO_4)_3$		$Rb_4Th(MoO_4)_4$		$Rb_4Th_5(MoO_4)_{12}$	
IR[a]	Raman	IR	Raman	IR	Raman	IR	Raman
(u)	(g)	(u)	(g)	(u)	(g)	(u)	(g)
916s[b]	912s (ν_1)	936s	949s (ν_1)	940m[c]	951w[d]	952m	984sh[e]
899sh	905w	926sh	937m		942s	940m	969m
886sh	896w		930s		936sh	930s	958s
			908m		908s (ν_1)	909sh	944s (ν_1)
			891m		903s (ν_1)	892w	932sh
			883m		881w		926m
							914sh
							888w
817sh	879m (ν_3)	895s	853s (ν_3)	880sh	869w	900sh	872m
800s	859m	846sh	798w	851s	858w	876s	863m
785sh	851sh	825sh	750w	791s	837m (ν_3)	835sh	856m
771m	843w	800s	703w	780sh	808m	813s	833sh
733s	793w	773s	674w	751s	796m	741sh	826m
	769w	703s		726s	779m		815m
	748sh				766m		807sh
	735w				740w		798m
							787s
							776m
							765m
							746s (ν_3)
	644w	623s	510w	626sh			
	481w						
436w	433w	494sh	466w	441w	467w	424w	410w
	394sh	463w	402m	418w	403w	409w	384w
	379m (ν_4)	416m	386m		390w		372w
	356m		369m		374sh		357m (ν_4)
	347m		353sh		371m		341m
	335s (ν_2)		343s (ν_4)		368m (ν_4)		331s (ν_4)
	328sh		318s (ν_2)		355w		321sh
	322m		309sh		344m		311m
	303s				331s		
					326m		
					324sh		
					319s (ν_2)		
					308m		
	288m		272m		288m		302sh
	191w		221w		252sh		284m
	157w		178m		238w		225w
	140w		167m		219w		205w
	123m		155s		185w		163w
			138m		173w		141w
			130m		149w		
					135w		
					127w		
	115sh		108s		112w		114w
	104w						

[a]The accuracy of all values is assumed to be ±1 cm^{-1}. Note that the bands assignment was carried out according to the previous literature data upon both solid-state and aqueous solution of MoO_4^{2-} groups. [b]s = strong. [c]m = medium. [d]w = weak. [e]sh = shoulder.

three band parts that are centered around 940 cm^{-1}, 820 cm^{-1}, and 420 cm^{-1} and correspond to ν_1, ν_3, and $\nu_2 + \nu_4$ modes of MoO_4^{2-}. Because $Rb_4Th_5(MoO_4)_{12}$ has the most vibrational modes, its infrared spectrum is less well-resolved, leading to a broadened spectrum. Table 2 exhibits the assignment of Raman and IR modes deduced from the spectra of this experiment and from a comparison with literature data on both solid-state and aqueous solution of MoO_4^{2-}.[20b,21] As noted above, each structure is based upon the similar ThO_8 square antiprism and MoO_4 tetrahedral units, and because of the flexibility of the Th−O−Mo connection, ThO_8 and MoO_4 fundamentals can combine in different ways to exhibit various structural forms. However, obviously, the coordination details of MoO_4 and ThO_8 are distinct in these structural forms. For example, in $Rb_8Th(MoO_4)_6$, the shortest Mo−O distance of 1.739(6) Å is longer than that of any of the other 3 rubidium thorium

dx.doi.org/10.1021/ic403003f | Inorg. Chem. 2014, 53, 3088−3098

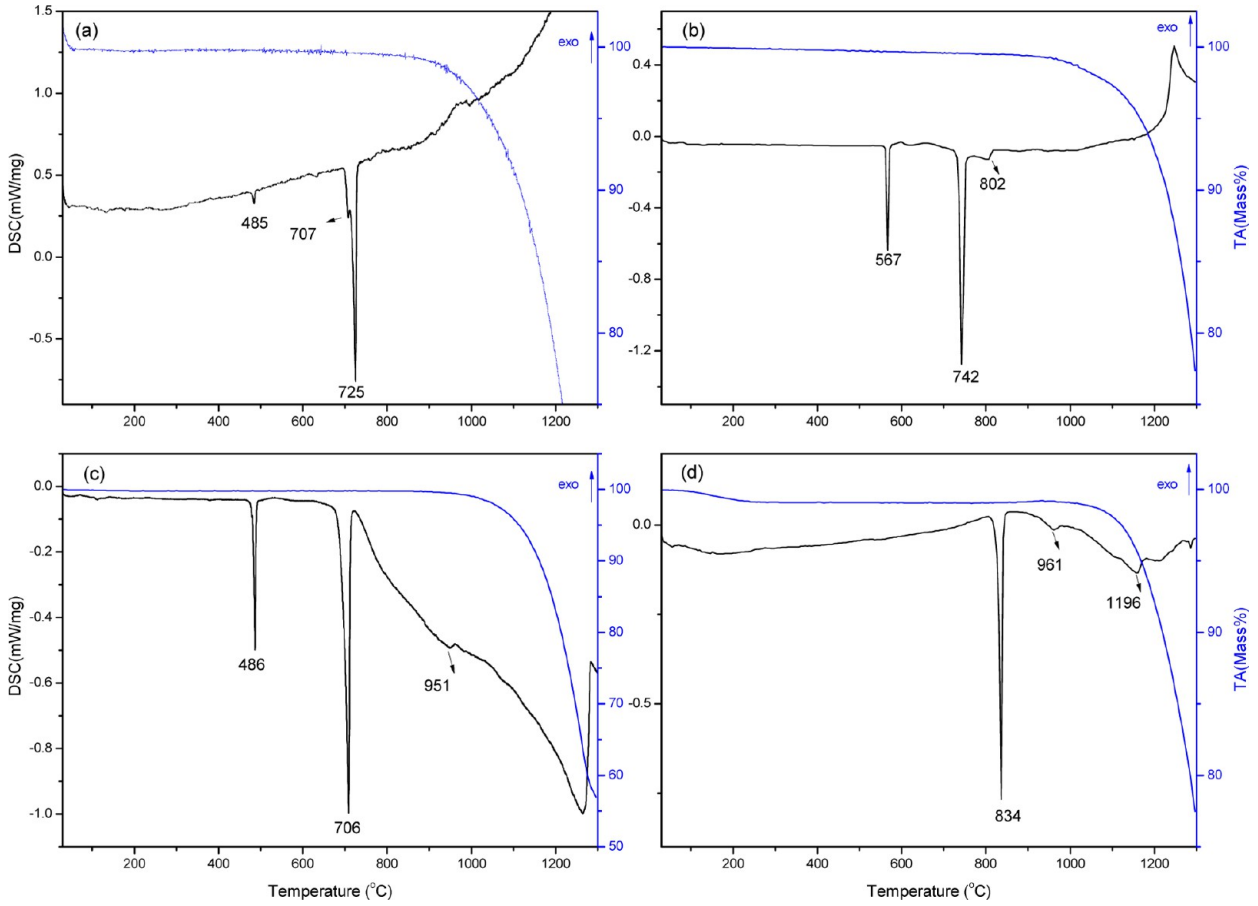

Figure 9. DSC (black) and TG (blue) curves of (a) $Rb_8Th(MoO_4)_6$, (b) $Rb_2Th(MoO_4)_3$, (c) $Rb_4Th(MoO_4)_4$, (d) $Rb_4Th_5(MoO_4)_{12}$.

molybdates, such as 1.716(3) Å in $Rb_4Th(MoO_4)_4$, 1.705(4) Å in $Rb_2Th(MoO_4)_3$, and 1.674(8) Å in $Rb_4Th_5(MoO_4)_{12}$. This means that the MoO_4 tetrahedra are distorted least in $Rb_8Th(MoO_4)_6$ and most in $Rb_4Th_5(MoO_4)_{12}$. This trend is consistent with the equation reported by Hardcastle and Wachs[22]

$$R_{Mo-O} = 0.48239 \ln(32895/\nu_1)$$

where the Mo−O bond length (R) was calculated as a function of ν_1. From the Raman spectra, the symmetric stretching modes ν_1 of $Rb_8Th(MoO_4)_6$ appear at lower wavenumbers, namely, 880−912 cm^{-1} compared to those in $Rb_2Th(MoO_4)_3$ (883−949 cm^{-1}), in $Rb_4Th(MoO_4)_4$ (881−951 cm^{-1}), and in $Rb_4Th_5(MoO_4)_{12}$ (888−984 cm^{-1}). Using the ν_1 values supplied in Table 2 (912(2) cm^{-1}, 949(2) cm^{-1}, 951(2) cm^{-1}, and 984(2) cm^{-1} for $Rb_8Th(MoO_4)_6$, $Rb_2Th(MoO_4)_3$, $Rb_4Th(MoO_4)_4$, and $Rb_4Th_5(MoO_4)_{12}$, respectively), the shortest Mo−O bond length can be calculated to be 1.730(1), 1.710(1), 1.709(1), and 1.693(1) Å, respectively, which is in agreement with the structure resolution results. As a consequence, we may conclude that the lower the wavenumber for stretching modes ν_1, the longer is the distance for the shortest Mo−O bond, and the more regular is the MoO_4 tetrahedron.

3.4. Thermal Properties and Phase Transitions. The thermal behavior of as-prepared pure phases obtained by TG-DSC on heat flow with temperatures between 30 and 1250 °C is shown in Figure 9. The peak located at 725(3) °C symbolizes the melting point of $Rb_8Th(MoO_4)_6$. A small endothermic peak detected at 485(3) °C can be attributed to impurities in $Rb_8Th(MoO_4)_6$ as these samples always show a very small amount (∼5% of total weight) of $Rb_4Th(MoO_4)_4$ during the powder synthesis. This endothermic peak becomes obvious in the DSC of $Rb_4Th(MoO_4)_4$. Three endothermic peaks of $Rb_2Th(MoO_4)_3$ were obtained during heating, with the onset points starting at 555(3), 720(3), and 774(3) °C. The highest peak corresponds to the solid−liquid transformation, and the following one, which shifts about 60 °C with regard to the corresponding endothermic peak, means the ending of the melting, with all the material becoming liquid. The most interesting behavior for $Rb_2Th(MoO_4)_3$ is the first endothermic event, because there is no obvious variation of weight loss, and it is reasonable to assume that the first peak results from the solid−solid phase transition of the $Rb_2Th(MoO_4)_3$ phase. $Rb_4Th(MoO_4)_4$ shows an incongruent melting starting at around 666(3) °C, with a maximum heat flow at 706(3) °C. In addition, a potential solid-phase transition feature is noticed at 486(3) °C. The broad endothermic behavior from approximately 715 °C to about 1210 °C may be attributed to the sample decomposition. For $Rb_4Th_5(MoO_4)_{12}$, a single sharp endothermic peak is located at 836(3) °C, which relates to the melting point of this phase. Similar to $Rb_2Th(MoO_4)_3$, the solid−liquid finishing point for $Rb_4Th_5(MoO_4)_{12}$ is evident, although the ending point of $Rb_4Th_5(MoO_4)_{12}$ is a little higher (961(3) °C). The TG curve indicates the melting product of $Rb_4Th_5(MoO_4)_{12}$ begins to evaporate at 1196(5) °C.

3.5. High-Temperature Powder Diffraction. In addition to the temperature-dependent behavior of the samples

dx.doi.org/10.1021/ic403003f | Inorg. Chem. 2014, 53, 3088−3098

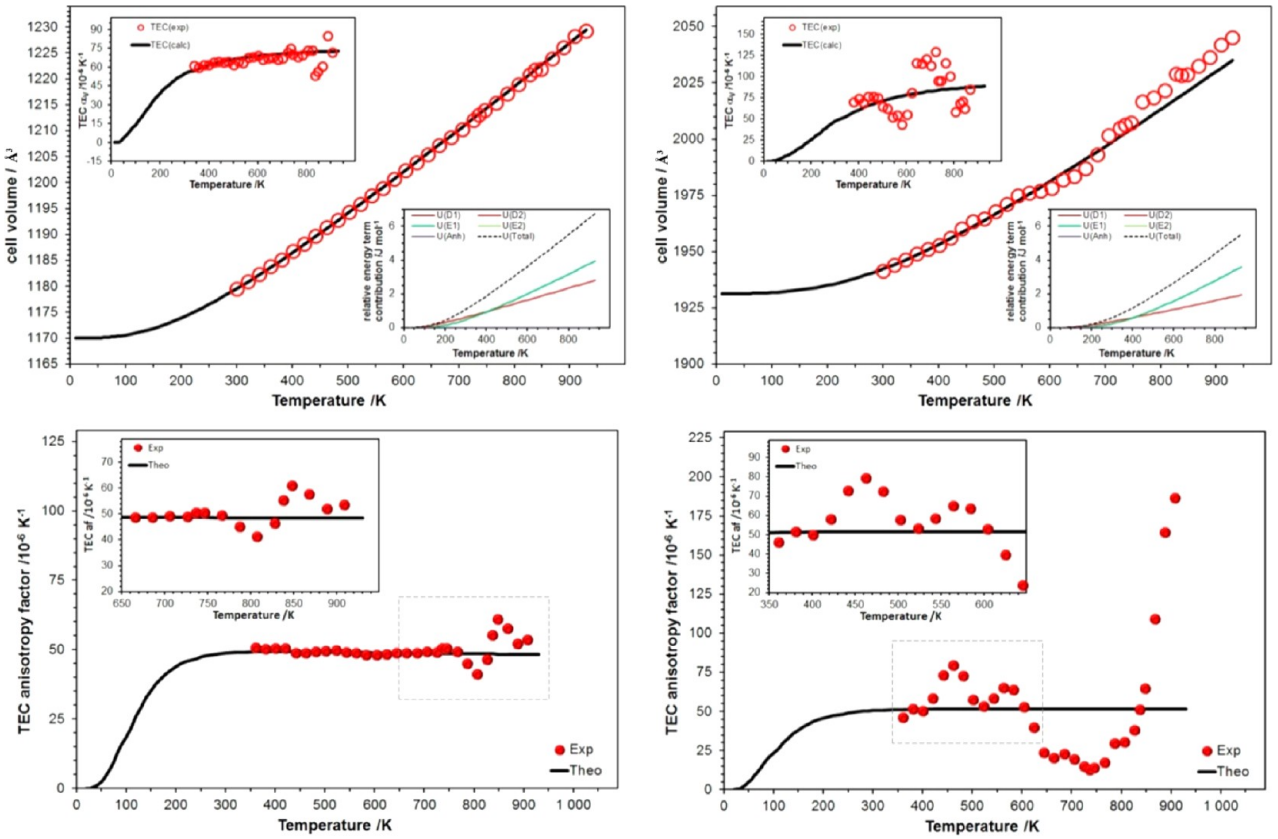

Figure 10. Temperature-dependent evolution of the unit cell-volume (upper row) of $Rb_2Th(MoO_4)_3$ (left) and $Rb_4Th(MoO_4)_4$ (right). The top left insets show the respective change of the thermal expansion coefficient (TEC); the bottom right ones show the expansion energy of the respective phonon contributions. In the lower part the anisotropy of the thermal expansion coefficients is given. The black lines correspond to the calculated values using a Debye-Einstein model.

investigated using TG-DSC analyses, high-temperature X-ray powder diffraction was used to further confirm the assumption of the phase-transition behavior of $Rb_2Th(MoO_4)_3$ and $Rb_4Th(MoO_4)_4$. The thermal volume expansion behavior was calculated (Figure 10) using the extended metric expression, taking the quasi-harmonic Debye U_{Di}, the harmonic Einstein U_{Ei}, and the anharmonic internal energy U_A contributions into account.[23] During the refinement the U_{D2}, U_{E2}, and U_A contributions were found to be zero. For $Rb_2Th(MoO_4)_3$, the values of V_0 = 1170.0(1) Å^3, k_{D1} = 1069(19) × 10^{-14} Å^3 K^{-1}, θ_{D1} = 419(7) K, k_{E1} = 1872(33) × 10^{-14} Å^3 K^{-1}, and θ_{E1} = 706(13) K were found. For $Rb_4Th(MoO_4)_4$ the same calculations were carried out to V_0 = 1931(10) Å^3, k_{D1} = 1699(187) × 10^{-14} Å^3 K^{-1}, θ_{D1} = 600(66) K, k_{E1} = 4544(499) × 10^{-14} Å^3 K^{-1}, and θ_{E1} = 1066(117) K. As seen from the standard deviations as well as in Figure 10, the model describes only slightly the temperature-dependent behavior of this compound up to about 277 °C (550 K). Therefore the calculated energy contributions should not be further used to calculate the internal energy. Nevertheless, the deviations from this equation as well as from the anisotropy of the thermal expansion coefficient (TEC), which was calculated using the internal energy equation, clearly show the dynamic of both phases. In $Rb_2Th(MoO_4)_3$ the TEC anisotropy factor (Figure 10) stays constant around 50(2) × 10^{-6} K^{-1} followed by an unsteady step beginning around 767 K, showing the maximum slope at 840 K (which corresponds well with the signal maximum of 567(3) °C in the DSC) and decreases to 52(2) × 10^{-6} K^{-1}. This is a clear indication for a structural change of $Rb_2Th(MoO_4)_3$ in this temperature range. Comparing the room-temperature pattern before and after the heating cycle up to 650 °C in $Rb_2Th(MoO_4)_3$, only a few very weak reflections disappear, which might be explainable by minor impurities. At the highest measured temperature slight changes in the intensities of the reflections are visible compared to the room-temperature pattern, which might serve as a hint for a displacive phase transition. Nevertheless, the changes are small, and within a few standard deviations no significant deviations could be calculated from the recorded powder data.

In $Rb_4Th(MoO_4)_4$ the TEC anisotropy behavior is much more pronounced (Figure 10). For this compound small deviations are seen between 400 and 600 K. These deviations have no counterpart in the DSC measurements, and therefore it is not clear if these effects are real or if there is only one or two motions, as might be deduced from the inset in the respective figure (Figure 10). On the other hand there is, after a decrease of the TEC anisotropy factor from about 22(2) × 10^{-6} K^{-1} to 12(2) × 10^{-6} K^{-1}, a rapid increase of these values starting at 760(10) K, which is at the same temperature as the endothermic DSC signal maximum at 486(3) °C. The increase of the TEC anisotropy factor reaches 186(2) × 10^{-6} K^{-1} at 910 K, which was the highest temperature measured before destroying the material. Also for $Rb_4Th(MoO_4)_4$ the pattern at room temperature looks (neglecting also here some minor impurities) the same before and after the measurement, and again the pattern at the highest measured temperature shows only small deviations in intensities; no significant deviations could be calculated from the recorded powder data.

dx.doi.org/10.1021/ic403003f | Inorg. Chem. 2014, 53, 3088−3098

CONCLUSIONS

In conclusion, four thorium rubidium molybdates, $Rb_8Th(MoO_4)_6$, $Rb_2Th(MoO_4)_3$, $Rb_4Th(MoO_4)_4$, and $Rb_4Th_5(MoO_4)_{12}$ were synthesized using high-temperature solid-state method. Apart from $Rb_4Th(MoO_4)_4$, which has been characterized by powder X-ray diffraction, no further structural detail has been reported in the literatures among thorium rubidium molybdates. These phases adopt different structure types from simple zero-dimensional to complex 3D structures, with remarkable dimensionality reduction along the $[Rb_2MoO_4]_x[Th(MoO_4)_2]_y$ series. Despite this fact, Th has only one type of oxygen coordination, that is, ThO_8 antiprism. Detailed spectroscopic analysis demonstrates that structural evolution effects in Raman and IR spectra of titled compounds. TG-DSC shows that two phases, $Rb_8Th(MoO_4)_6$ and $Rb_4Th_5(MoO_4)_{12}$, keep the same structure until melting. The temperature-dependent X-ray powder diffraction data analysis confirms phase transitions of $Rb_2Th(MoO_4)_3$ and $Rb_4Th(MoO_4)_4$ corresponding to the endothermic TG-DSC. Nevertheless, the deviations are really small and the high-temperature structures could not be finally evaluated from powder data (which is not surprising due to the large unit-cell volume of each phase).

ASSOCIATED CONTENT

Supporting Information

This includes compound structures in cif files, images, tables, and spectra. This material is available free of charge via the Internet at http://pubs.acs.org.

AUTHOR INFORMATION

Corresponding Author

*E-Mail: e.alekseev@fz-juelich.de.

Notes

The authors declare no competing financial interest.

ACKNOWLEDGMENTS

The authors are grateful to the Helmholtz Association for funding within the VH-NG-815 project. T.M.G. especially acknowledges the "Deutsche Forschungsgemeinschaft" DFG for the support within the Heisenberg program (GE1981/3-1).

REFERENCES

(1) (a) Bagla, P. *Science* **2005**, *309*, 1174. (b) Kazimi, M. S. *Am. Sci.* **2003**, *91*, 408. (c) Şahin, S.; Özceyhan, V.; Yapici, H. *Ann. Nucl. Energy* **2001**, *28*, 203. (d) Sinha, R. K.; Kakodkar, A. *Nucl. Eng. Des.* **2006**, *236*, 683.

(2) (a) Underwood, C. C.; Mann, M.; McMillen, C. D.; Kolis, J. W. *Inorg. Chem.* **2011**, *50*, 11825. (b) Krivovichev, S. V.; Burns, P. C. *J. Solid State Chem.* **2002**, *168*, 245. (c) Krivovichev, S. V.; Finch, R. J.; Burns, P. C. *Can. Mineral.* **2002**, *40*, 193.

(3) (a) Alekseev, E. V.; Krivovichev, S. V.; Armbruster, T.; Depmeier, W.; Suleimanov, E. V.; Chuprunov, E. V.; Golubev, A. V. *Z. Anorg. Allg. Chem.* **2007**, *633*, 1979. (b) Cross, J. N.; Duncan, P. M.; Villa, E. M.; Polinski, M. J.; Babo, J.-M.; Alekseev, E. V.; Booth, C. H.; Albrecht-Schmitt, T. E. *J. Am. Chem. Soc.* **2013**, *135*, 2769. (c) Suleimanov, E. V.; Golubev, A. V.; Alekseev, E. V.; Geiger, C. A.; Depmeier, W.; Krivovichev, V. G. *J. Chem. Thermodyn.* **2010**, *42*, 873.

(4) (a) Alekseev, E. V.; Krivovichev, S. V.; Malcherek, T.; Depmeier, W. *Inorg. Chem.* **2007**, *46*, 8442. (b) Alekseev, E. V.; Suleimanov, E. V.; Chuprunov, E. V.; Golubev, A. V.; Fukin, G. K.; Marychev, M. O. *Russ. J. Inorg. Chem.* **2007**, *52*, 1446. (c) Krivovichev, S. V.; Cahill, C. L.; Burns, P. C. *Inorg. Chem.* **2003**, *42*, 2459. (d) Obbade, S.; Yagoubi, S.; Dion, C.; Saadi, M.; Abraham, F. *J. Solid State Chem.* **2003**, *174*, 19.

(5) Freundlich, W. P. M. *C. R. Acad. Sci.* **1969**, *269*, 392.

(6) Thoret, J. *Rev. Chim. Miner.* **1974**, *11*, 237.

(7) Tabuteau, A.; Pages, M. *J. Inorg. Nucl. Chem.* **1980**, *42*, 401.

(8) (a) Huyghe, M.; Lee, M. R.; Jaulmes, S.; Quarton, M. *Acta Crystallogr., Sect. C: Cryst. Struct. Commun.* **1993**, *49*, 950. (b) Huyghe, M.; Lee, M. R.; Quarton, M.; Robert, F. *Acta Crystallogr., Sect. C: Cryst. Struct. Commun.* **1991**, *47*, 244. (c) Huyghe, M.; Lee, M. R.; Quarton, M.; Robert, F. *Acta Crystallogr., Sect. C: Cryst. Struct. Commun.* **1991**, *47*, 1797.

(9) (a) N.N.Bushuev, V. K. T. *Zh. Neorg. Khim.* **1975**, *20*, 1143. (b) N.N.Bushuev, V. K. T. *Zh. Neorg. Khim.* **1975**, *20*, 1233. (c) Bushuev, N. T. *Dokl. Chem.* **1974**, *217*, 533.

(10) Dahale, N. D.; Keskar, M.; Singh Mudher, K. D. *J. Alloys Compd.* **2006**, *415*, 244.

(11) Keskar, M.; Sali, S. K.; Dahale, N. D.; Krishnan, K.; Kulkarni, N. K.; Phatak, R.; Kannan, S. *J. Nucl. Mater.* **2013**, *438*, 15.

(12) Sheldrick, G. *Acta Crystallogr., Sect. A: Found. Crystallogr.* **2008**, *64*, 112.

(13) Brese, N. E.; O'Keeffe, M. *Acta Crystallogr., Sect. B: Struct. Sci.* **1991**, *47*, 192.

(14) (a) Xiao, B.; Huang, Y.; Zhang, L.; Lin, Z.; Wang, G. *PLoS One* **2012**, *7*, e40229. (b) Yu, Y.; Huang, Y.; Zhang, L.; Lin, Z.; Wang, G. *PLoS One* **2013**, *8*, e54450.

(15) Efremov, V. A.; Trunov, V. K.; Berezina, T. A., *Kristallografiya* **1982**, *27*.

(16) Efremov, V. A.; Berezina, T. A.; Averina, I. M.; Trunov, V. K., *Kristallografiya* **1980**, *25*.

(17) Launay, S.; Jaulmes, S.; Lucas, F.; Quarton, M. *J. Solid State Chem.* **1998**, *136*, 199.

(18) Long, J. R.; McCarty, L. S.; Holm, R. H. *J. Am. Chem. Soc.* **1996**, *118*, 4603.

(19) Tulsky, E. G.; Long, J. R. *Chem. Mater.* **2001**, *13*, 1149.

(20) (a) Klimin, S. A.; Popova, M. N.; Mavrin, B. N.; van Loosdrecht, P. H. M.; Svistov, L. E.; Smirnov, A. I.; Prozorova, L. A.; von Nidda, H. A. K.; Seidov, Z.; Loidl, A.; Shapiro, A. Y.; Demianets, L. N. *Phys. Rev. B* **2003**, *68*, 174408. (b) Mąaczka, M.; Paraguassu, W.; Souza Filho, A. G.; Freire, P. T. C.; Melo, F. E. A.; Mendes Filho, J.; Hanuza, J. *J. Raman Spectrosc.* **2005**, *36*, 56.

(21) (a) Mahadevan Pillai, V. P.; Pradeep, T.; Bushiri, M. J.; Jayasree, R. S.; Nayar, V. U. *Spectrochim. Acta, Part A* **1997**, *53*, 867. (b) Busey, R. H.; Keller, J. O. L. *J. Chem. Phys.* **1964**, *41*, 215.

(22) Hardcastle, F. D.; Wachs, I. E. *J. Raman Spectrosc.* **1990**, *21*, 683.

(23) (a) Murshed, M. M.; Gesing, T. M. *Mater. Res. Bull.* **2013**, *48*, 3284. (b) Gesing, T. M.; Mendive, C. B.; Curti, M.; Hansmann, D.; Kalita, P. E.; Lipinska, K. E.; Cornelius, A. L.; Murshed, M. M.; Huq, A.; Nénert, G. *Z. Kristallogr.* **2013**, *228*, 532.